

Main Manuscript for

Band Gap Opening of Metallic Single-Walled Carbon Nanotubes via Noncovalent Symmetry Breaking

Authors: Francesco Mastrocinque,¹ George Bullard,¹ James A. Alatis,¹ Joseph A. Albro,³ Animesh Nayak,¹ Nicholas X. Williams,² Amar Kumbhar,⁴ Hope Meikle^{1,2} Zachary X. W. Widel,¹ Yusong Bai,¹ Alexis K. Harvey,⁵ Joanna M. Atkin,⁵ David H. Waldeck,³ Aaron D. Franklin^{1,2} and Michael J. Therien^{1*}

Affiliation: ¹Department of Chemistry, Duke University, Durham, North Carolina, 27708, United States. ²Department of Electrical & Computer Engineering, Duke University, Durham, North Carolina 27708, United States. ³Department of Chemistry, University of Pittsburgh, Pittsburgh, Pennsylvania, 15260, United States. ⁴Chapel Hill Analytical & Nanofabrication Laboratory, University of North Carolina, Chapel Hill, North Carolina, 27599, United States. ⁵Department of Chemistry, University of North Carolina, Chapel Hill, North Carolina, 27599, United States.

*Correspondence to: michael.therien@duke.edu

Author Contributions:

Conceptualization: F.M., G.B., Y.B., M.J.T

Investigation: F.M., G.B., J.A.A., J.A.A., A.N., N.X.W., A.K., H.M., Z.X.W., A.K.H.

Formal Analysis: F.M., G.B., J.A.A., J.A.A., A.N., N.X.W., A.K., A.K.H., J.M.A.

Funding acquisition: J.M.A., D.H.W., A.D.F., M.J.T.

Project administration: M.J.T.

Supervision: J.M.A., D.H.W., A.D.F., M.J.T.

Writing – original draft: F.M., G.B., M.J.T.

Writing - review & editing: Y.B., D.H.W., A.D.F., M.J.T.

Competing Interest Statement: The authors declare no competing interest.

Classification: Physical Sciences: Chemistry

Keywords: Single-Walled Carbon Nanotubes, Band gap opening, Symmetry breaking

This PDF file includes:

Main Text Figures 1 to 4 Table 1

Abstract

Covalent bonding interactions determine the energy-momentum (E-k) dispersion (band structure) of solid-state materials. Here we show that noncovalent interactions can modulate the E-k dispersion near the Fermi level of a low-dimensional nanoscale conductor. We demonstrate that low energy band gaps may be opened in metallic carbon nanotubes through polymer wrapping of the nanotube surface at fixed helical periodicity. Electronic spectral, chiro-optic, potentiometric, electronic device, and work function data corroborate that the magnitude of band gap opening depends on the nature of the polymer electronic structure. Polymer dewrapping reverses the conducting-to-semiconducting phase transition, restoring the native metallic carbon nanotube electronic structure. These results address a long-standing challenge to develop novel carbon nanotube electronic structures that are not realized through disruption of π conjugation, and establish a roadmap for designing and tuning specialized semiconductors that feature band gaps on the order of a few hundred meV.

Significance Statement

Metallic carbon nanotubes are one-dimensional tubular structures made up of hexagonally bonded sp² carbon atoms. We show that by wrapping a metallic nanotube surface with rigid polymers, a semiconductor can be realized. This strategy contrasts approaches that regulate electronic structural properties of bulk-phase materials which rely on altering the nature of covalent bonding. Reversible non-covalent polymer wrapping of metallic carbon nanotubes interconverts metallic and semiconducting electronic structures. Because the energy separation between carbon nanotube valence and conduction bands depends on the polymer electronic structure, this work provides a new approach to realize novel low band gap one-dimensional materials by design.

Main Text

Introduction

Single-walled carbon nanotubes (SWNTs) offer unique mechanical, thermal, optical, and electronic properties for diverse applications (1-4). SWNTs, for example, display superior charge carrier mobilities relative to conventional microelectronic materials such as Si and GaAs (5), and their π-conduction pathways are impervious to electromigration, which is an important source of failure as device size decreases (6). SWNT properties are intimately linked to their lattice structure, which can be modeled as a cylindrical sheet of graphene rolled-up along a specific direction, given by a pair of roll-up indices (*n*, *m*). Depending on the roll-up indices, a SWNT can be metallic (m-SWNT) or semiconducting (s-SWNT). The nanotube's electronic structure can be related to graphene by using the zone folding approximation and accounting for perturbations arising from the nanotube curvature and roll up vector (7). Unlike graphene's electronic band structure (Fig. 1A), which is characterized by Dirac points that touch at the K and K' manifolds in the 2D graphene E-k dispersion curves, SWNTs display periodic boundary conditions that result in a series of allowed wave vectors in reciprocal space (*K*-space) known as quantization lines. The intersection (Fig. 1B) or displacement (Fig. 1C) of these quantization lines with the *K* or *K'* manifolds determines whether a given nanotube is metallic or semiconducting.

Production of SWNTs with targeted electronic properties defines a longstanding challenge. Controlled band gap opening of m-SWNTs provides a potential route to engineering unique nanotube electronic structures. Theory suggests two methods to open band gaps in m-SWNTs: (i) orchestrating asymmetric interfacial nanotube sidewall interactions that promote

symmetry breaking (8), and (ii) creating nanotube electronic perturbations that emerge from heteroatom doping (9-12). Related to these predictions, recent work shows that covalent modification of the nanotube lattice in a DNA/s-SWNT hybrid assembly leads to new modes of low-energy electronic excitation (13). Such covalent modification or heteroatom doping of the SWNT lattice, however, also leads to the introduction of trap sites that can disrupt fundamental SWNT electronic properties, such as ballistic transport (14-16).

In this work, we show that low-energy band gaps on the order of a few hundred meV can be introduced in m-SWNTs by breaking nanotube sublattice symmetry through rigorously controlled noncovalent interactions. We demonstrate reversible m-to-s-SWNT phase transitions for three unique semiconducting polymer-wrapped (11,11) SWNT hybrid assemblies, and characterize their properties through optical, potentiometric, chiroptical, and electronic device data. This m-SWNT noncovalent modification strategy relies on regulation of the nature of interfacial electronic interactions between the m-SWNT lattice with an ordered, rigid, conjugated organic semiconducting polymer that helically wraps the SWNT surface at fixed periodicity and constant morphology. In these supramolecular nanostructures, specific regions of the SWNT sp²hybridized lattice electronically mix with the conjugated polymeric wrapper, while other regions do not. This introduction of a controlled and periodic asymmetric environment on the m-SWNT lattice enforced by the conjugated polymer electronic structure affects K and K' point displacement from the allowed quantization lines in the first Brillouin zone (Fig. 1D) and drives a metal-tosemiconductor phase transition in the nanotube. These findings open a potent pathway to break nanotube sublattice symmetry and thus create new low band gap one-dimensional nanoscale optoelectronic materials.

Results and Discussion

Symmetry breaking in (11,11) m-SWNTs via conjugated, helical polymer wrapping. We developed binaphthalene-based, aryleneethynylene semiconducting polymer designs that exfoliate, individualize, and disperse SWNTs through chiral, single-chain helical wrapping at a fixed pitch length, which ensure morphological homogeneity of the resultant polymer-SWNT superstructures (17-20). Highly-enriched (11.11) m-SWNTs were isolated and purified using aqueous two-phase extraction (ATPE) techniques (see Materials and Methods), and subsequently wrapped with S-PBN(b)-Ph4, R-PBN(b)-Ph3, and R-PBN(b)-Ph3-PDI polymers, generating polymer-wrapped S-PBN(b)-Ph₄-[(11,11) SWNTs], R-PBN(b)-Ph₃-[(11,11) SWNTs], and R-PBN(b)-Ph₃-PDI-[(11,11) SWNTs] (Fig. 2). Note that S-PBN(b)-Ph₄ and R-PBN(b)-Ph₃ polymers have nearly-identical potentiometrically determined HOMO and LUMO energy levels and maintain a near-identical pitch length on the (11,11) SWNT surface (~9 nm) as measured by transmission electron (TEM) and atomic force microscopy (AFM), while wrapping the SWNT with opposite helical handedness (Table 1; Supplementary Figs. S4-S5 and S12-S13). The R-PBN(b)-Ph₄-PDI polymer wraps the (11,11) SWNT surface with a slightly longer pitch length (~11 nm) and possesses HOMO and LUMO energies distinct from those of the S-PBN(b)-Ph4 and R-PBN(b)-Ph₃ polymers (Table 1). The set of S-PBN(b)-Ph₄-[(11,11) SWNT], R-PBN(b)-Ph₃-[(11,11) SWNT], and R-PBN(b)-Ph₃-PDI-[(11,11) SWNT] nanoscale superstructures was used to examine the extent to which these polymer electronic structures break (11,11) m-SWNT lattice symmetry. For these studies, (11,11) m-SWNTs dispersed in water using an achiral sodium dodecyl sulfate surfactant (1% SDS) provided a control sample.

Optical determination of (11,11) m-SWNT band gap opening via Fourier-transform infrared (FT-IR) spectroscopy. Fourier-transform infrared (FT-IR) spectra of these polymer-m-SWNT superstructures in water and deuterium oxide solvents demonstrate distinct optical signatures in the polymer-wrapped (11,11) SWNT assemblies that are completely absent in the SDS-dispersed (11,11) m-SWNTs and unbound polymer spectra. S-PBN(b)-Ph₄-[(11,11) SWNT] (Fig. 3a) and *R*-PBN(b)-Ph₃-[(11,11) SWNT] superstructures show new IR transitions at similar energies, centered at 2450 cm⁻¹ (0.30 eV) and 2150 cm⁻¹ (0.27 eV), respectively. In contrast, the polymer-

wrapped *R*-PBN(b)-Ph₃-PDI-[(11,11) SWNT] sample shows a new IR absorption signature that is higher in energy than those evinced for the *S*-PBN(b)-Ph₄-[(11,11) SWNT] and *R*-PBN(b)-Ph₃-[(11,11) SWNT] assemblies, centered at 3340 cm⁻¹ (0.42 eV). The new infrared transitions manifest only in the polymer-wrapped (11,11) SWNT assemblies, and are not present in the FT-IR spectra of the polymer itself or the SDS-dispersed (11,11) m-SWNT samples. Moreover, these new IR transitions, which are induced by polymer wrapping the m-SWNT surface at a fixed helical pitch length, vanish under experimental conditions that cause polymer unwrapping (Supplementary Fig. S21).

Cyclic voltametric (CV) measurements of (11,11) m-SWNT band gap opening. Congruent with the FT-IR data, potentiometric measurements of the polymer-SWNT superstructures indicate band gap opening in (11,11) SWNTs upon polymer-wrapping. Polymer- and SDS-dispersed (11,11) m-SWNT assemblies were drop-cast onto a glassy carbon working electrode (see Materials and Methods). The potentiometric band gaps in the polymer-SWNT structures were determined through cyclic voltammetric (CV) measurements (Fig. 3b) using approaches described previously (21-23). These experiments revealed potentiometric band gaps for the S-PBN(b)-Ph₄-[(11,11) SWNT], *R*-PBN(b)-Ph₃-[(11,11) SWNT], and *R*-PBN(b)-Ph₃-PDI-[(11,11) SWNT] superstructures which mirror those determined by FT-IR spectroscopy. For the SDS-dispersed (11,11) m-SWNTs, the observed current-voltage responses obtained in these CV experiments were congruent with those expected for a metallic nanotube sample (24).

Bottom-gate field-effect transistors (FETs) demonstrating a metal-to-semiconductor electronic transition in (11,11) SWNTs. To further highlight that rigid semiconducting polymer wrapping of the (11,11) SWNT surface at a fixed helical periodicity enforces a semiconducting electronic structure by lifting the degeneracy of adjacent sites in the SWNT unit cell, substrategated field-effect transistors (FETs) were fabricated using aerosol jet printing (25, 26). For the thin-film channel material, either the S-PBN(b)-Ph4-[(11,11) SWNTs] or the SDS-dispersed [(11,11) m-SWNTs] were printed onto previously formed Ag nanoparticle (AgNP) contacts (Fig. 3c). The drain current (I_D) was monitored while sweeping the applied gate-source voltage (V_{GS}) from -60 V to 60 V and maintaining a fixed drain-source voltage of 500 mV. Figure 3d shows the results of this experiment, in which the current is plotted as a ratio of I_D and the maximum current (I_{max}) . These data underscore the significant difference in $I_{max}I_{min}$ ratios between the SDSdispersed [(11,11) m-SWNTs] (I_{max}/I_{min} = 1) and the S-PBN(b)-Ph₄-[(11,11) SWNTs] (I_{max}/I_{min} = 10). The FET devices also exhibited remarkable differences in conductivity, with the m-SWNT device current (10-6 µA) three orders of magnitude larger than the S-PBN(b)-Ph₄-[(11,11) SWNT]based FET (10-9 µA). It is not expected that the metal-to-semiconductor electronic transition that is driven by S-PBN(b)-Ph₄ wrapping of the (11,11) SWNT surface would lead to such a dramatic reduction in conductivity. Rather, the lower current is attributed to increased resistance at the nanotube junctions across the transistor channel (27). Since these thin-film transistors have channel lengths of 250 um, the current transports from source to drain along a tube-to-tube percolation path. While the difference in junction resistance between nanotubes in the two FET devices would not be expected to yield an increase in the gate modulation, it can yield differences in channel conductivity. Despite the increased resistivity of the thin films, the only source for increased gate modulation in the S-PBN(b)-Ph₄-[(11,11) SWNTs] FET is the opening of a band gap in the channel material (Fig. 3d).

Measuring changes in work function using Kelvin-Probe Force Microscopy (KPFM). Further quantification of (11,11) SWNT band gap opening and electronic structure modulation via helical polymer wrapping was elucidated through Kelvin probe force microscopy (KPFM) measurements (Fig. 4a,b). A metal-to-semiconductor phase transition should cause a change in the measured work function. To determine work functions of SDS-dispersed and polymer-wrapped [(11,11) SWNTs] from measurements of contact potential difference (V_{CPD}), the AFM tip was calibrated using the known work function of HOPG (ϕ_{HOPG} = 4.6 eV) (28, 29). The work function of the SDS-dispersed (11,11) m-SWNTs was determined to be 4.72 eV, in line with previously established

values for the m-SWNT work function (30). The polymer-SWNT work functions were measured to be 5.14 eV for *R*-PBN(b)-Ph₃-PDI-[(11,11) SWNTs], 5.04 eV for *R*-PBN(b)-Ph₃-[(11,11) SWNTs], and 5.05 eV for *S*-PBN(b)-Ph₄-[(11,11) SWNTs]; note that these values track with the extent of band gap opening determined in the optical and potentiometric experiments (Table 1).

Characterizing Changes in SWNT Raman modes concomitant with band gap opening. Raman spectroscopy provides an approach to investigate the degree of SWNT lattice strain imparted by polymer-wrapping of the m-SWNT surface. Unlike the Raman G-band of graphite, which exhibits a singular Lorentzian-shaped signature corresponding to the tangential lattice vibrations of the carbon atoms, the SWNT G-band is composed of two main components, termed G⁺ and G⁻ (31). The SWNT G⁺ band arises from lattice vibrations of carbon atoms along the SWNT longitudinal axis, whereas the G⁻ band derives from lattice vibrations of carbon atoms along the SWNT circumferential direction. Differences in the line shapes, spectral frequencies, and intensity ratios of the SWNT G⁺ and G⁻ Raman active modes provide information about the spatial lattice curvature and electronic structure of a given SWNT (32).

The G-signature of SDS-dispersed (11,11) m-SWNTs, centered at 1559 cm⁻¹, displays a broad Breit-Wigner-Fano lineshape, while the G⁺ signature, centered at 1584 cm⁻¹, displays a sharp Lorentzian lineshape (Fig. 4c). In addition, the relative G⁺/G⁻ intensity ratio of the SDSdispersed (11,11) m-SWNTs is approximately unity. The lineshape of the G⁺ and G⁻ modes, coupled with the relative G⁺/ G intensity, resemble previously established Raman G-mode responses of SWNTs that are metallic (31, 33, 34). In contrast, all of the polymer-wrapped (11,11) SWNT assemblies display diminished G-intensities compared to SDS-dispersed (11,11) m-SWNTs, consistent with benchmark Raman characterization data for semiconducting SWNTs (35-37). Note that the intensities of the D bands of the SDS-dispersed (11,11) m-SWNT, R-PBN(b)-Ph₃-[(11,11) SWNT], S-PBN(b)-Ph₄-[(11,11) SWNT] and R-PBN(b)-Ph₃-PDI-[(11,11) SWNT] samples are indistinguishable, indicating that defect densities in these m-SWNT systems are all identical. These data thus highlight that this G- and G+ signature modulation stemming from symmetry breaking derives from polymer-wrapping of the m-SWNT surface at fixed helical pitch length that drives a metallic-to-semiconducting transition, and cannot be ascribed to the potential introduction of new defect sites into the SWNT lattice during polymer wrapping or the purification and isolation procedures.

Confirmation of (11,11) m-SWNT symmetry breaking via circular dichroism (CD) spectroscopy. Chiro-optic confirmation of symmetry breaking of the (11,11) m-SWNT lattice via polymer-wrapping was further corroborated via circular dichroism (CD) spectroscopy (Fig. 4d). SDS-dispersed (11,11) m-SWNTs display no CD signal in the M₁₁ transition manifold, as expected given the achiral, armchair lattice structure which characterizes these samples. In contrast, *R*-PBN(b)-Ph₃-[(11,11) SWNT], S-PBN(b)-Ph₄-[(11,11) SWNT] and *R*-PBN(b)-Ph₃-PDI-[(11,11) SWNT] superstructures display CD signals in the M₁₁ transition manifold. These data highlight that: (i) wrapping (11,11) m-SWNTs with polymers having identical electronic structures but opposite helical handedness (*R*-PBN(b)-Ph₃ and S-PBN(b)-Ph₄) display CD signals that depend on absolute semiconducting polymer chirality, and (ii) symmetry breaking, enforced by a semiconducting polymer wrapping the SWNT surface at a fixed helical pitch length, drives displacement of SWNT excited-state electron density along a helically chiral path.

Conclusions

Metal-to-semiconductor phase transitions have been demonstrated in (11,11) m-SWNTs. Symmetry breaking of the (11,11) m-SWNT electronic structure was accomplished through single-chain polymer-wrapping of the nanotube surface and confirmed through a combination of FT-IR, Raman, CD, potentiometric, KPFM, and FET device experimental data. Regulating the electronic structure of the polymer that helically wraps the m-SWNT surface modulates the

magnitude of band gap opening over a 0.27 to 0.42 eV range in these exemplary *R*-PBN(b)-Ph₃-[(11,11) SWNT], S-PBN(b)-Ph₄-[(11,11) SWNT] and *R*-PBN(b)-Ph₃-PDI-[(11,11) SWNT] superstructures. Reversible, noncovalent symmetry breaking of metallic carbon nanotubes via rigid single-chain helical polymer-wrapping enables design of novel low energy band gap materials. This work thus defines a new approach for engineering 1D nanoscale compositions having bespoke electronic and optical responses.

Materials and Methods

Additional details regarding the synthesis of polymer structures, materials characterization, and optical and electronic measurements may be found in the Supplementary Information,

Materials. All manipulations were carried out under argon previously passed through an O2 scrubbing tower (Schweitzerhall R3-11G catalyst) and a drying tower (Linde 13X molecular sieves) unless otherwise stated. Air sensitive solids were handled in a Braun 150-M glove box. Standard Schlenk techniques were employed to manipulate air-sensitive solutions. Tetrahydrofuran (THF), CH₂Cl₂, N,N-dimethylformamide (DMF), methanol, and diethylether were collected from a PURE SOLV (Innovative Technology) solvent purification system. Dioxane and triethylamine were distilled from Na/4-benzoylbiphenyl and NaOH pellets, respectively, under argon; diisopropylamine was purchased from Aldrich and re-distilled. All NMR solvents were used as received. The catalysts PdCl₂(PPh₃)₂, Pd(PPh₃)₄ and [PddppfCl₂] were purchased from Strem Chemicals and used as received, 1,3-Propane sultone, phenylacetylene, 4-iodophenol, (triisopropylsilyl)acetylene, triethylene glycol monomethyl ether, enantiopure (ee 99%) (R)-(-)-1,1'-bi(2-naphthol) and enantiopure (ee 99%) (S)-(-)-1,1'-bi(2-naphthol) were purchased from Aldrich and used without further purification. Neat bromine and tetra-nbutylammoniumfluoride (TBAF) were purchased from Aldrich and used as received. Perylene-3,4,9,10-tetracarboxylic dianhydride and 2.5-Dibromohydroquinone were purchased from AK Scientific and used as received. IsoNanotubes-M % metallic enriched SWNTs were obtained from Nano Integris as a suspension and used as a starting material. Flash and size exclusion column chromatography were performed on the bench top, using respectively silicagel (EM Science, 230-400 mesh) and Bio-Rad Bio-Beads SX-1 in THF.

Instrumentation. Free, unbound polymer in each polymer/SWNT sample was removed using a GE/ÄKTApurifier HPLC system (GE Healthcare Bio-Science AB, Björkgatan, Uppsala, Sweden) equipped with two preparative columns (160x16 mm each; stationary phase: sephacryl S-500 and S-200) connected in a series. The HPLC system uses three-wavelength detection, which distinguishes fractions that contain SWNTs. Electronic spectra were recorded on a Varian 5000 UV/vis/NIR spectrophotometry system. Atomic force microscopy (AFM; Digital Instruments Dimension 3100) images were obtained via intermittent contact mode (scan rate = 0.6 Hz. ambient temperature) using super-sharp Si-tips (FORTA-SS-10 from AppNano; tip radius < 5 nm, cantilever resonant frequency ~70 kHz). AFM samples were prepared by drop-casting SWNT suspensions on Si wafer surfaces (cleaned with acetone and 2-propanol); such samples were then desiccator-dried for overnight. AFM data are presented with a 1st order plane fit. NMR spectra were recorded on either a 400 or 500 MHz AC-Bruker spectrometer. Chemical shifts for ¹H NMR spectra are relative to residual protium in deuterated solvent (CDCl₃ = 7.26 ppm, D₂O = 4.75 ppm). All J values are reported in Hertz. MALDI-TOF mass spectroscopic data were obtained with a Perspective Voyager DE instrument (Department of Chemistry, Duke University). Microwave-assisted reactions were performed using an Emrys Personal Chemistry System (Biotage). Transmission electron microscopy images (JEOL TEM-2010; accelerate voltage, 200 kV) were obtained from samples prepared via drop casting on lacy Formvar copper grids stabilized with carbon, followed by drying in a desiccator overnight.

FET Device Fabrication. P++ silicon with a 300 nm SiO₂ oxide was used to fabricate the transistors. The silicon substrate was used as a gate. Before printing, the silicon chips were first ultrasonicated in isopropanol (IPA) for 10 minutes, rinsed with deionized (DI) water, and dried with nitrogen (N₂), then ultrasonicated in acetone for 10 minutes, rinsed with DI water, and dried with N₂. Source and drain electrodes were printed using silver nanoparticles (AgNPs). To enable printing, terpinol was added to the ink at a 9:1 ratio of ink:terpinol. The printer platen temperature was held constant at 60 °C throughout the duration of AgNP printing. The printing parameters were held at an atomizer flow rate of 30 SCCM, a sheath flow rate of 25 SCCM, an ultrasonic current of 350 mA, and a 150 μm nozzle was used. After printing, the AgNPs traces were sintered at 200 °C for 1 hour. For SWNT printing, the printer platen and the ink bath temperature were held at 20 °C. An atomizer flow rate of 23 SCCM, a sheath flow rate of 40 SCCM, an ultrasonic current of 350 mA, and a nozzle diameter of 150 μm was used for printing. After deposition, the SWNTs were held in an 80 °C DI water bath for 10 minutes. 1 pass of SWNTs was used in all testing. All devices have a channel length of 250 μm and a channel width of 200 μm.

Potentiometric Measurements. A standard three-electrode configuration was used, involving a glassy carbon working electrode, a platinum wire counter electrode, and a Ag/AgCl (3M KCl) reference electrode. electrode was separated from the bulk solution by a junction bridge filled with the corresponding solvent/electrolyte solution. Measurements were repeated using a fluorine-doped tin oxide working electrode. Electrochemical measurements were performed using tetra-n-butylammoniumhexafluorophosphate (TBAPF $_6$; 0.1 M) as the supporting electrolyte in anhydrous CH $_2$ Cl $_2$ solvent under an argon atmosphere. Each ionic polymer-wrapped [(11,11) SWNT] solution (7:3 H $_2$ O: MeOH was dropcast (5 μ Lx7) onto the working electrode, evaporated under a stream of N $_2$ gas, and then dried under vacuum. For each polymer wrapped [(11,11) SWNT] sample, cathodic and anodic half cycles (100 mV/s) were scanned separately. Each scan was repeated three times and the onset potentials for reduction or oxidation were determined using established electrochemical characterization methods for conjugated semiconducting polymers (21, 22).

Optical Spectroscopy. For all optical measurements (Raman, IR, and CD spectroscopy), both the SDS-dispersed and polymer-wrapped samples were prepared in aqueous solutions ($OD_{M11} = 0.3$). All spectroscopic measurements were carried out at 23 ± 1 °C.

Raman Spectroscopy. Samples were excited using a 633 nm (HeNe) laser line. Spectra were collected over a 200 – 2000 cm⁻¹ measurement window using a 40 second acquisition time with 6 accumulations. The instrument was calibrated using Si-based solid-state calibration sample.

FT-IR Spectroscopy. H₂O and D₂O solution-phase samples were placed onto the diamond ATR crystal using 0.2 mL of solution. Data was acquired using 32 scans over a 1000 – 4000 cm⁻¹ range.

CD Spectroscopy. Solution-phase samples were acquired as a single scan over a 300-800 nm range using a step size of 1 nm.

AFM and KPFM Measurements. Samples were prepared by drop-casting SWNT suspensions onto Au-coated Si wafer surfaces (cleaned with acetone and 2-propanol); such samples were then dried via solvent evaporation for 3 h. AFM images were collected via intermittent contact mode (scan rate = 0.6 Hz, ambient temperature). KPFM probes were calibrated using freshly cleaved HOPG (ϕ_{HOPG} = 4.6 eV)(28, 29) to determine the work function of the probe. A dilute aqueous solution of each SWNT sample was drop casted onto the surface of a 100 nm Au substrate and the work function of each sample determined using two-pass KPFM. All data were evaluated using standard functions in the SPM data analysis software, Gwyddion 2.59 (38).

Transmission Electron Microscopy Measurements. Samples were prepared via dropcasting on lacy Formvar copper grids stabilized with carbon followed by drying in desiccators overnight and collected using a voltage acceleration between 150 - 200 kV.

Chirality Enriched (11,11) m-SWNTs. IsoNanotubes-M-98% were concentrated to 0.1 mg/mL in aqueous 1.04% deoxycholate (DOC) using Millipore regenerated cellulose ultrafiltration discs (100 kDa NMW). To a centrifuge tube, 4.8 mL of IsoNanotubes-M-98% (0.1 mg/mL) in 1.04% DOC, 10 mL of 20% Dextran (70K), 25 mL of 25% PEG (6K), and 5 mL of H₂O were added. The centrifuge tube was shaken vigorously and centrifuged for 3 minutes at 3300 rpm. 5 mL of the bottom phase was extracted and placed into a new centrifuge tube with 10 mL of 4% SC, and 10 mL 25% PEG (6K). The centrifuge tube was shaken vigorously and centrifuged for 3 minutes at 3300 rpm. The light blue-green bottom phase containing single-chirality enriched (11,11) SWNTs was extracted from the centrifuge tube and stored in a separate vial. (11,11) SWNTs: M_{11} = 690 nm.

General Polymer-Wrapping Procedure. A procedure identical to that previously published was employed (17, 19, 39-41). An aqueous suspension of chirality enriched [(11,11) SWNTs] (4 mL; OD = 0.5) was added over a course of 3 h to a 10 mL solution of the corresponding polymer (3:7 MeOH:H₂O, 0.5 mg/ml). The mixture was stirred overnight and was exchanged into a 5 mM carbonate/15 mM NaCl buffer (pH ~9) using a Microcon centrifugal filter YM-100 (Millipore, Bedford, MA). Free, unbound polymer was removed via gel permeation chromatography: a 2 mL polymer-SWNT solution (SWNT concentration of ~0.5 mg/ml) was injected into a series of two preparative columns (160x16 mm each) loaded with sephacryl-based separatory medium connected in the order of S-500 and S-200, and eluted with a 5 mM carbonate/15 mM NaCl buffer in 3:7 MeOH:H₂O at a flow rate of 1 ml/min; three-wavelength detection (for all samples, carbon nanotubes were detected at 580 nm; phenylene-based polymers were detected at 315 and 440 nm) was used to identify fractions that did not contain nanotubes. The fractions were collected as 1 mL aliquots; the polymer-SWNT fractions eluted at an earlier time (19-27 min range) followed by the free, unbound polymer (28-48 min range; see Figure S6). Polymer-SWNT-containing fractions (eluting over an 19-27 min range) were collected together and desalted via centrifuging through a Microcon centrifugal filter YM-100 (Millipore, Bedford, MA) while washing (~4x5 ml) with an aqueous solvent mixture (4:6 CH3CN/D2O) containing no salt. The volume of the polymer-wrapped [(11,11) SWNTs] solution was adjusted to 4 mL (4:6 CH₃CN/D₂O) and the pH was adjusted to ~8 by adding an appropriate amount of 0.1 mM NaOD in D₂O.

General Polymer De-Wrapping Procedure. An aqueous suspension of polymer-wrapped [(11,11) SWNTs] (0.5 mL; OD > 0.1) was dropcast onto a Si wafer and placed in an oven at 450 °C for 12 hours. The wafer was then removed from the oven, cooled to room temperature, and redispersed into a 1% SDS aqueous solution (0.3 mL) to generate the polymer de-wrapped (11,11) m-SWNT sample.

Acknowledgments

F.M., G.B., J.A.A., A.N., H.M., Z.X.W.W., Y.B., and M.J.T. acknowledge the Air Force Office of Scientific Research (FA9550-18-1-0222) for funding this research. N.X.W. and A.D.F. acknowledge the National Institutes of Health (1R01HL146849), J.A.A. and D.H.W acknowledge the United States National Science Foundation (CHE-2140249), and A.K.H. and J.M.A. acknowledge the National Science Foundation Graduate Research Fellowship (DGE-2040435) for research support. M.J.T is grateful to the John Simon Guggenheim Memorial Foundation for a research fellowship.

References

- 1. S. M. Bachilo *et al.*, Structure-assigned optical spectra of single-walled carbon nanotubes. *Science* **298**, 2361-2366 (2002).
- 2. L. J. Carlson, T. D. Krauss, Photophysics of individual single-walled carbon nanotubes. *Acc. Chem. Res.* **41**, 235-243 (2008).
- 3. P. Avouris, Z. Chen, V. Perebeinos, Carbon-based electronics. *Nat. Nanotechnol.* **2**, 605-615 (2010).
- 4. Q. Cao *et al.*, Arrays of single-walled carbon nanotubes with full surface coverage for high-performance electronics. *Nat. Nanotechnol.* **8**, 180-186 (2013).
- 5. X. Zhou, J.-Y. Park, S. Huang, J. Liu, P. L. McEuen, Band structure, phonon scattering, and the performance limit of single-walled carbon nanotube transistors. *Phys. Rev. Lett.* **95**, 146805 (2005).
- 6. T. Taychatanapat, K. I. Bolotin, F. Kuemmeth, D. C. Ralph, Imaging electromigration during the formation of break junctions. *Nano Lett.* **7**, 652-656 (2007).
- 7. X. Blase, L. X. Benedict, E. L. Shirley, S. G. Louie, Hybridization effects and metallicity in small radius carbon nanotubes. *Phys. Rev. Lett.* **72**, 1878 (1994).
- 8. P. Delaney, H. J. Choi, J. Ihm, S. G. Louie, M. L. Cohen, Broken symmetry and pseudogaps in ropes of carbon nanotubes. *Nature* **391**, 466-468 (1998).
- 9. V. H. Crespi, M. L. Cohen, A. Rubio, In Situ Band Gap Engineering of Carbon Nanotubes. *Phys. Rev. Lett.* **79**, 2093-2096 (1997).
- 10. V. V. Ivanovskaya, A. Zobelli, O. Stéphan, P. R. Briddon, C. Colliex, BN Domains Included into Carbon Nanotubes: Role of Interface. *J. Phys. Chem. C* **113**, 16603-16609 (2009).
- 11. M. Qiu *et al.*, Band gap opening and semiconductor—metal phase transition in (n, n) single-walled carbon nanotubes with distinctive boron—nitrogen line defect. *Phys. Chem. Chem. Phys.* **18**, 4643-4651 (2016).
- 12. Z. J. Li, L. Wang, Y. J. Su, P. Liu, Y. F. Zhang, Semiconducting single-walled carbon nanotubes synthesized by S-doping. *Nano-Micro Lett.* **1**, 9-13 (2009).
- 13. Z. Lin *et al.*, DNA-guided lattice remodeling of carbon nanotubes. *Science* **377**, 535-539 (2022).
- 14. I. S. Esqueda *et al.*, The impact of defect scattering on the quasi-ballistic transport of nanoscale conductors. *J. Appl. Phys.* **117**, 084319 (2015).
- 15. X. M. Liu, H. E. Romero, H. R. Gutierrez, K. Adu, P. C. Eklund, Transparent Boron-Doped Carbon Nanotube Films. *Nano Lett.* **8**, 2613-2619 (2008).
- 16. U. N. Maiti *et al.*, 25th Anniversary Article: Chemically Modified/Doped Carbon Nanotubes & Graphene for Optimized Nanostructures & Nanodevices. *Adv. Mater.* **26**, 40-67 (2014).
- 17. P. Deria *et al.*, Single-handed helical wrapping of single-walled carbon nanotubes by chiral, ionic, semiconducting polymers. *J. Am. Chem. Soc.* **135**, 16220-16234 (2013).
- 18. C. D. Von Bargen *et al.*, Origins of the helical wrapping of phenyleneethynylene polymers about single-walled carbon nanotubes. *J. Phys. Chem. B* **117**, 12953-12965 (2013).
- 19. P. Deria, J.-H. Olivier, J. Park, M. J. Therien, Potentiometric, Electronic, and Transient Absorptive Spectroscopic Properties of Oxidized Single-Walled Carbon Nanotubes Helically Wrapped by Ionic, Semiconducting Polymers in Aqueous and Organic Media. *J. Am. Chem. Soc.* **136**, 14193-14199 (2014).

- 20. J.-H. Olivier *et al.*, Unambiguous Diagnosis of Photoinduced Charge Carrier Signatures in a Stoichiometrically Controlled Semiconducting Polymer-Wrapped Carbon Nanotube Assembly. *Angew. Chem. Int. Ed.* **54**, 8133-8138 (2015).
- 21. C. M. Cardona, W. Li, A. E. Kaifer, D. Stockdale, G. C. Bazan, Electrochemical considerations for determining absolute frontier orbital energy levels of conjugated polymers for solar cell applications. *Adv. Mater.* **23**, 2367-2371 (2011).
- W. Talsma et al., Efficient Selective Sorting of Semiconducting Carbon Nanotubes Using Ultra-Narrow-Band-Gap Polymers. ACS Appl. Mater. Interfaces 14, 38056-38066 (2022).
- 23. M. L. Gross, M. A. Hickner, Using Cyclic Voltammetry to Measure Bandgap Modulation of Functionalized Carbon Nanotubes. *Electrochem. Solid-State Lett.* **13**, K5 (2010).
- A. Al-Zubaidi et al., Cyclic Voltammogram Profile of Single-Walled Carbon Nanotube Electric Double-Layer Capacitor Electrode Reveals Dumbbell Shape. J. Phys. Chem. C 116, 7681-7686 (2012).
- 25. N. X. Williams, G. Bullard, N. Brooke, M. J. Therien, A. D. Franklin, Printable and recyclable carbon electronics using crystalline nanocellulose dielectrics. *Nat. Electron.* **4**, 261-268 (2021).
- 26. J. A. Cardenas *et al.*, In-Place Printing of Carbon Nanotube Transistors at Low Temperature. *ACS Appl. Nano. Mater.* **1**, 1863-1869 (2018).
- 27. N. F. Zorn, J. Zaumseil, Charge transport in semiconducting carbon nanotube networks. *Appl. Phys. Rev.* **8** (2021).
- 28. C. Sommerhalter, T. W. Matthes, T. Glatzel, A. Jäger-Waldau, M. C. Lux-Steiner, Highsensitivity quantitative Kelvin probe microscopy by noncontact ultra-high-vacuum atomic force microscopy. *Appl. Phys. Lett.* **75**, 286-288 (1999).
- 29. W. N. Hansen, G. J. Hansen, Standard reference surfaces for work function measurements in air. *Surf. Sci.* **481**, 172-184 (2001).
- 30. C. Chun-Wei, L. Ming-Hsien, Dependence of workfunction on the geometries of single-walled carbon nanotubes. *Nanotechnology* **15**, 480 (2004).
- 31. A. Jorio, R. Saito, Raman spectroscopy for carbon nanotube applications. *J. Appl. Phys.* **129**, 021102 (2021).
- 32. B. Gao, Y. Zhang, J. Zhang, J. Kong, Z. Liu, Systematic comparison of the Raman spectra of metallic and semiconducting SWNTs. *J. Phys. Chem. C* **112**, 8319-8323 (2008).
- 33. K. Vasu *et al.*, Opening of large band gaps in metallic carbon nanotubes by mannose-functionalized dendrimers: experiments and theory. *J. Mater. Chem. C* **6**, 6483-6488 (2018).
- 34. M. S. Dresselhaus, A. Jorio, M. Hofmann, G. Dresselhaus, R. Saito, Perspectives on Carbon Nanotubes and Graphene Raman Spectroscopy. *Nano Lett.* **10**, 751-758 (2010).
- 35. F. Toshimitsu, N. Nakashima, Semiconducting single-walled carbon nanotubes sorting with a removable solubilizer based on dynamic supramolecular coordination chemistry. *Nat. Commun.* **5**, 5041 (2014).
- 36. J. Lefebvre *et al.*, High-Purity Semiconducting Single-Walled Carbon Nanotubes: A Key Enabling Material in Emerging Electronics. *Acc. Chem. Res.* **50**, 2479-2486 (2017).
- 37. J. Wang *et al.*, Growing highly pure semiconducting carbon nanotubes by electrotwisting the helicity. *Nat. Catal.* **1**, 326-331 (2018).
- 38. D. Nečas, P. Klapetek, Gwyddion: an open-source software for SPM data analysis. *Open Physics* **10** (2012).

- 39. G. Depotter *et al.*, First-order hyperpolarizabilities of chiral, polymer-wrapped single-walled carbon nanotubes. *Chem. Commun.* **52**, 12206-12209 (2016).
- 40. Y. Bai, J.-H. Olivier, G. Bullard, C. Liu, M. J. Therien, Dynamics of charged excitons in electronically and morphologically homogeneous single-walled carbon nanotubes. *Proc. Natl. Acad. Sci. U.S.A.* **115**, 674-679 (2018).
- 41. Y. Bai, G. Bullard, J.-H. Olivier, M. J. Therien, Quantitative Evaluation of Optical Free Carrier Generation in Semiconducting Single-Walled Carbon Nanotubes. *J. Am. Chem. Soc.* **140**, 14619-14626 (2018).

Figure Legends:

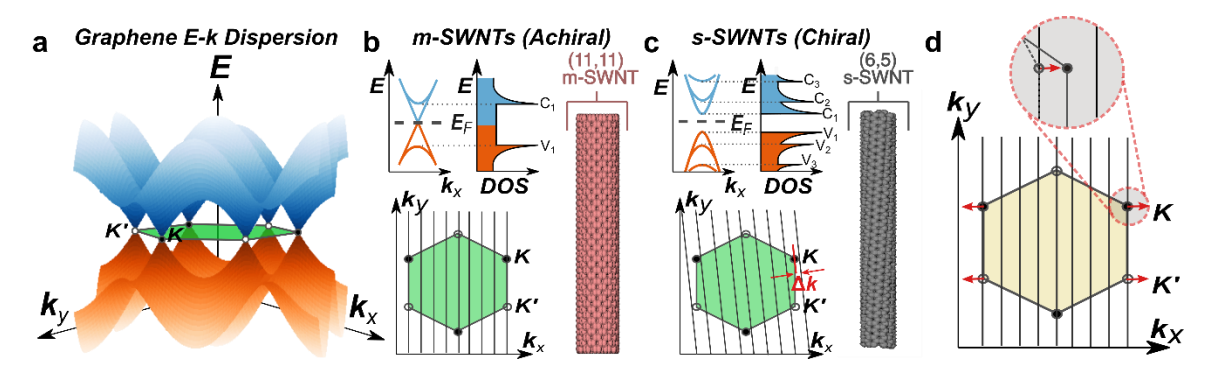


Figure 1 | Carbon nanotube electronic structure and noncovalent symmetry breaking. a, E-k dispersion diagram of graphene. **b,c**, Linear E-k dispersion relation, density of states, and first Brillioun zone of an achiral armchair (11,11) m-SWNT and a chiral (6, 5) s-SWNT. The quantization lines in the first Brillioun zone bypass (s-SWNT) or intersect (m-SWNT) the K and K' points and determine the SWNT electronic structure. The magnitude of the s-SWNT band gap is proportional to the minimum separation of a K or K' point and its nearest quantization line, denoted as Δk. **d**, Illustrations of Dirac point shifting driven by symmetry breaking resulting in m-SWNT band gap opening.

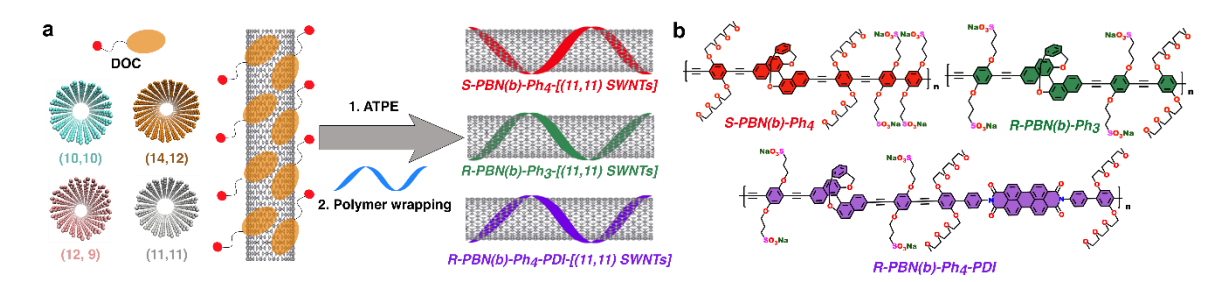


Figure 2 | Generation of hybrid, polymer-wrapped (11,11) m-SWNT superstructure assemblies. a, Polymer-wrapping of aqueous two-phase extraction (ATPE)-purified (11,11) m-SWNTs dispersed in sodium deoxycholate (DOC). b, Molecular structures of the chiral, polyanionic semiconducting polymers used to helically wrap the (11,11) m-SWNT nanotube lattice.

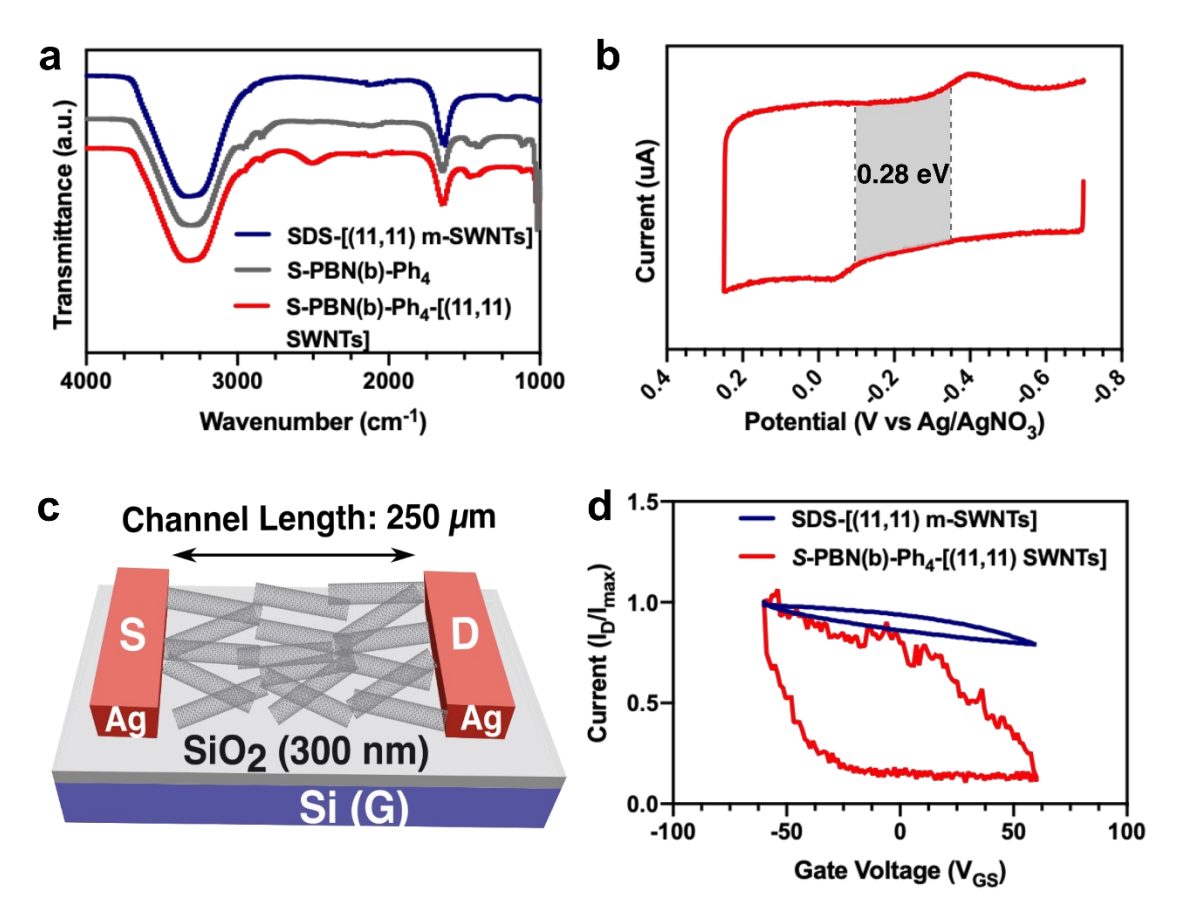


Figure 3 | Demonstrating m-SWNT band gap opening via helical wrapping of the nanotube surface with a rigid semiconducting polymer at fixed periodicity. a, FT-IR measurements demonstrating an IR transition (2450 cm⁻¹) for the *S*-PBN(b)-Ph₄-[(11,11) SWNTs] that is absent for the bare (11,11) SWNT and *S*-PBN(b)-Ph₄ polymer components. **b,** Cyclic voltametric data acquired for *S*-PBN(b)-Ph₄-[(11,11) SWNT] superstructures demonstrating a 0.28 eV band gap. **c,** Illustration of a printed FET device structure and **d,** respective I_D-V_{GS} measurements taken at a fixed drain-source voltage of 500 mV highlighting the semiconducting behavior of a *S*-PBN(b)-Ph₄-[(11,11) SWNT]-based device compared to an analogous device fabricated from bare (11,11) m-SWNTs.

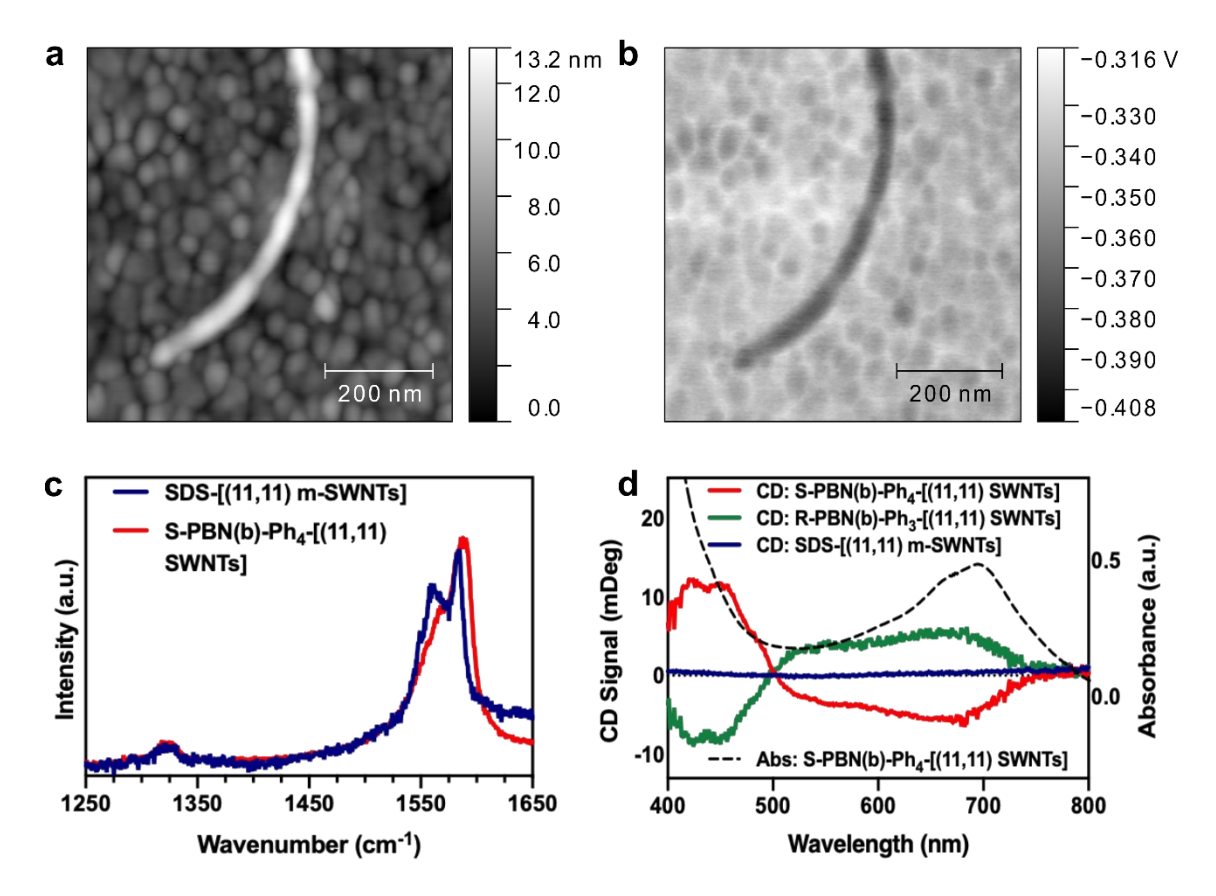


Figure 4 | Optical and electronic measurements of band gap opening in (11,11) m-SWNTs. a,b Topographic AFM image and KPFM potential map of the *R*-PBN(b)-Ph₃-PDI-[(11,11) SWNTs] demonstrating the ~0.36 eV difference in work function relative to the Au-coated AFM tip. **c**, Representative Raman spectra delineating the relative difference in G⁺/G⁻ intensities and lineshapes between SDS-dispersed and polymer-wrapped (11,11) SWNTs. **d**, CD spectra highlighting the chiro-optic confirmation of symmetry breaking in the polymer-wrapped *S*-PBN(b)-Ph₄-[(11,11) SWNT] (red trace) and *R*-PBN(b)-Ph₃-[(11,11) SWNT] (green trace) superstructures. No symmetry breaking is enforced in the achiral SDS-dispersed [(11,11) m-SWNTs] (blue trace); S-PBN(b)-Ph₄-[(11,11) SWNT], *R*-PBN(b)-Ph₃-[(11,11) SWNT], and SDS-dispersed (11,11) SWNT samples feature superimposable M₁₁ electronic transition manifolds (dotted line).

Table 1. Summary of metrical parameters, and spectroscopic, potentiometric, and work function data that confirm band gap opening of (11,11) m-SWNTs through symmetry breaking driven by nanotube surface wrapping by rigid helically chiral semiconducting

polymers.

polymers.							
Assembly	Polymer Pitch Length (nm) ^a	Potentiometric Band Gap (eV) ^b	Optical Band Gap (eV) ^c	Absolute W _F (eV) ^d	ΔW _F (eV) ^d	Raman G ⁺ /G ⁻ Intensity ^e	Optical CD Score (mdeg/OD) ^f
S-PBN(b)- Ph ₄ -[(11,11) SWNTs]	9.2	0.28	0.3	5.05	0.33	1.42	-44
R-PBN(b)- Ph ₃ -[(11,11) SWNTs]	9.0	0.26	0.27	5.04	0.32	1.38	+41
R-PBN(b)- Ph ₄ -PDI- [(11,11) SWNTs]	11.3	0.40	0.42	5.14	0.42	1.53	+51
SDS- dispersed [(11,11) m- SWNTs]	-	-	-	4.72	-	1.12	-

^aPolymer pitch lengths measured using high-resolution transmission electron microscopy (HR-TEM). ^bDetermined from the difference in oxidation and reduction onset potentials via cyclic voltammetry. ^cDetermined from the optical signature characteristic of the polymer-wrapped m-SWNT identified by FT-IR. ^dMeasured using KPFM with a calibrated Au tip. ΔW_F corresponds to the measured W_F difference between the polymer-wrapped (11,11) SWNT structure and that determined for SDS-dispersed (11,11) m-SWNTs. ^eG⁺ and G⁻ intensities determined using a 633 nm light source. ^fConcentration-normalized chiro-optic responses.